

Article

Method for Quantitative Broadband Diffuse Optical Spectroscopy of Tumor-Like Inclusions

Sandhya Vasudevan ¹, Farnoush Forghani ², Chris Campbell ¹, Savannah Bedford ¹ and Thomas D. O'Sullivan ^{1,*} 

¹ Department of Electrical Engineering, University of Notre Dame, Notre Dame, IN 46556, USA; svasude1@nd.edu (S.V.); ccampb19@nd.edu (C.C.); sbedford@nd.edu (S.B.)

² Department of Radiation Oncology, University of Colorado, School of Medicine, Aurora, CO 80045, USA; FARNOUSH.FORGHANI-ARANI@cuanschutz.edu

* Correspondence: tosullivan@nd.edu; Tel.: +1-574-631-4287

Received: 31 December 2019; Accepted: 15 February 2020; Published: 20 February 2020



Featured Application: This work describes a new hybrid diffuse optical imaging (DOI) method that extracts broadband optical properties of deep tumor-like inhomogeneities with a simple handheld probe more accurately than the conventional topographic DOI methods. This method is applicable to human breast tumor diagnosis as it can be used to characterize breast lesions by revealing enhanced optical information.

Abstract: A hybrid reflectance-based diffuse optical imaging (DOI) technique combining discrete wavelength frequency-domain (FD) near-infrared spectroscopy (NIRS) with broadband continuous wave NIRS measurements was developed to quantify the broadband optical properties of deep tumor-like inclusions. This method was developed to more accurately measure the broadband optical properties of human tumors using a compact handheld imaging probe and without requiring a priori spectral constraints. We simulated the reconstruction of absorption and scattering spectra (650–1000 nm) of human breast tumors in a homogeneous background at depths of 0 to 10 mm. The hybrid DOI technique demonstrated enhanced performance in reconstruction of optical absorption with a mean accuracy over all 71 wavelengths of 8.39% versus 32.26% for a 10 mm deep tumor with the topographic DOI method. The new hybrid technique was also tested and validated on two heterogeneous tissue-simulating phantoms with inclusion depths of 2, 7, and 9 mm. The mean optical absorption accuracy over all wavelengths was similarly improved up to 5x for the hybrid DOI method versus topographic DOI for the deepest inclusions.

Keywords: diffuse optical spectroscopy; hyperspectral diffuse optical imaging; hybrid frequency-domain (FD) continuous-wave (CW) method; diffuse optical imaging; multispectral imaging; broadband imaging

1. Introduction

In diffuse optical imaging (DOI), near-infrared (NIR) light is used to noninvasively probe cm-thick biological tissues to map macroscopic structure and function. For example, DOI can identify the distribution and concentrations of NIR tissue optical absorbers, such as oxy-, deoxy-hemoglobin, water, and lipids, and has been widely explored in clinical breast cancer applications [1–3]. These studies have demonstrated quantitative analysis of breast tissue (tumor and normal) composition [2,4–6], monitoring, and prediction of tumor response to chemotherapy [3,7,8] and differential diagnosis of malignant from benign lesions [9–13]. DOI techniques also provide advantages in terms of cost, safety, and accessibility as a point-of-care technology compared to other breast imaging methods [14].

Although many DOI systems use just a few optical wavelengths, several studies have shown that the accuracy of chromophore estimation is significantly affected by the lack of spectral information [15,16]. This is especially true when a targeted chromophore lies in an undersampled spectral region [16]. Therefore, broadband methods have been developed in the field of diffuse optics to broaden the wavelength range and provide accurate assessments of additional tissue constituents. For example, a broadband time-resolved diffuse optical spectrometer that measures absorption and scattering spectra of turbid media over the 600 to 1350 nm range was recently described [17]. The optical bandwidth of discrete wavelength quantitative frequency-domain (FD) NIR spectroscopy has also been expanded by combining it with broadband continuous-wave (CW) NIR spectroscopy in a hybrid instrument [1,16,18,19], or by using wavelength-tunable lasers [20].

However, because of instrument complexity, broadband DOI typically samples the tissue with limited (few or single) views and homogeneous models of tissue composition are employed. This results in a 2D spatial map of the optical “topography” of the tissue, and ignores any depth-dependent variations in tissue composition. This longstanding challenge in the field of diffuse optics leads to significant errors in optical property estimation of tissue inhomogeneities, such as breast tumors or in layered tissues such as the brain/skull/scalp. This error is the result of the partial volume effect, wherein the tissue inhomogeneity occupies only a small portion of the optically interrogated volume, and is one of the major limitations of employing homogeneous tissue models for optical property estimation [21,22].

A common alternative approach to imaging more complex tissues is diffuse optical tomography (DOT), which requires many DOI measurements at different tissue views and source–detector separations to reconstruct the 3D optical properties with tomographic algorithms. Indeed, studies of DOT techniques and applications [23,24] have employed spectrally constrained reconstruction techniques and have demonstrated improvements in the chromophore concentration recovery in the tissue. The spectral constraint DOT reconstruction algorithm, where instead of estimating optical properties at each wavelength independently, measurements at all wavelengths are coupled together to estimate chromophore concentrations directly given their known extinction spectra [25]. The spectral constraint in DOT reduces the number of unknowns, thereby making the inversion problem better posed, and is an excellent approach when the expected chromophores are known a priori. However, the spectral constraint approach is not suitable for applications when there are unknown chromophore contributions to the broadband absorption spectrum. For example, several studies have shown that the spectral shape and strength of unknown optical absorbers in breast tissue are a strong discriminator of benign and malignant breast lesions [9–13].

Therefore, the goal of this study was to develop a DOI technique that is capable of accurately measuring the 3D broadband optical properties of heterogeneous turbid media without having to employ spectral constraints. Specifically, we sought a technique that provides more accurate analysis of localized buried inhomogeneities, such as tumors, compared to 2D topographic DOI, but without the complexity and long computational times required for typical DOT methods. We restricted the interrogation geometry to reflection-based imaging so as to be applicable to a wide range of noninvasive tissue imaging applications and compact instrument configurations. This work is further motivated by and supports our efforts to create an ultraportable and fast handheld breast imager with few source–detector separations that can be scanned across the tissue to generate high density measurements [26]. As a result, we present a new hyperspectral hybrid FD- and CW-DOI methodology, implemented with a simple probe configuration, that enables broadband 3D optical property recovery without a priori spectral constraints [1]. Because reconstructing each wavelength individually with traditional DOT approaches greatly increases computational time, a limited number of 3D regions were specified from a priori spatial information where optical properties are expected to be different (i.e., the so-called hard spatial constraint). This spatial prior information is intended to be acquired through a separate structural imaging technique, such as ultrasound, which is compatible with reflectance-mode DOI [4,27]. Furthermore, discrete-wavelength FD measurements were chosen to accurately and directly

estimate the tissue optical scattering, which are used to constrain broadband CW measurements. The new hybrid technique allows for reconstruction of the optical properties in heterogeneous media over a wavelength range of 650 to 1000 nm from a simple grid of single source–detector measurements.

In this paper, we describe this hybrid DOI technique and study its accuracy using computational modeling and real tissue-simulating phantoms. The computational models simulate an ellipsoidal deep-tissue heterogeneity with optical properties mimicking a human breast tumor. We compare these results to optical properties recovered using conventional topographic DOI, where homogeneous models are employed. We also evaluate the approach experimentally using heterogeneous tissue-simulating phantoms with inclusions that recapitulate a breast tumor.

2. Materials and Methods

2.1. Hyperspectral Hybrid Frequency-Domain (FD) and Continuous-Wave (CW) Diffuse Optical Imaging DOI

The proposed hybrid FD/CW method is a three-step process starting with capturing quantitative FD measurements at multiple tissue views over the tumor-containing heterogeneous tissue. In this paper, the FD measurements were acquired at a limited number of wavelengths (660, 690, 785, and 830 nm), which were used to recover optical reduced scattering μ'_s and calculate a reliable prefactor (a) and power (b) by fitting the data to the empirical Mie scattering relationship $\mu'_s(\lambda) = a\left(\frac{\lambda}{500\text{ nm}}\right)^{-b}$ [28,29].

In the hybrid problem, we adopt the Finite Element Method (FEM)-based scheme and implemented it by NIRFAST software [30,31] to solve the inverse problem. The goal of the inverse problem is to recover optical properties of the tissue/medium, which is accomplished via an iterative optimization/minimization scheme, which seeks the minimum misfit between the measured and estimated data (represented by an objective function). In the hybrid method, FEM-based reconstructions are performed with hard priors of tumor location and size. In this research, we have confined our study to two region reconstructions, where optical properties are reconstructed for normal and tumor regions of the tissue. In hard prior reconstructions, the tissue volume can be segmented into multiple regions by appropriately labeling all nodes within each region [31]. This in turn reduces the dimensions of the Jacobian (sensitivity matrix), thereby making it a smaller well-conditioned matrix [31].

In the second step of the hybrid method, μ'_s was estimated for each CW wavelength from the recovered a and b for wavelengths in the spectral range 650 nm to 1000 nm at every 5 nm. In the final step, the broadband $\mu'_s(\lambda)$ were used to constrain CW recovery based on multiple broadband reflectance measurements to extract the optical absorption spectrum $\mu_a(\lambda)$. This approach mimics a hybrid FD/CW technique used in conventional topographic DOI imaging for homogeneous tissue [16]. Figure 1a depicts the hybrid method overview, and Figure 1b demonstrates an example of $\mu_a(\lambda)$ and $\mu'_s(\lambda)$ estimation of a simulated 0 mm deep ellipsoidal inhomogeneity (20 mm × 30 mm × 20 mm) using the FD and CW combined method.

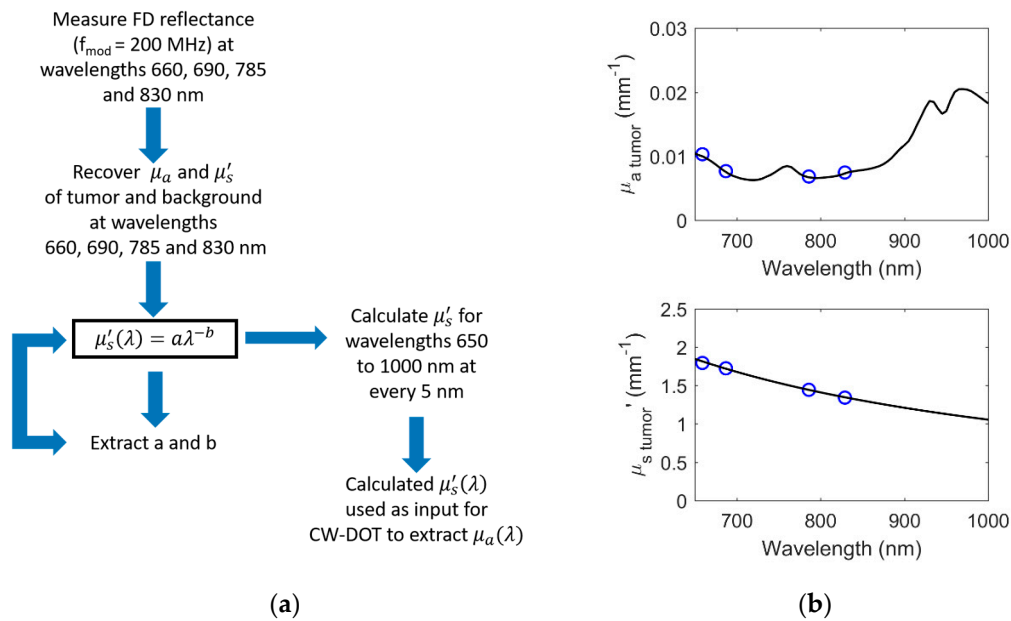


Figure 1. Hybrid frequency-domain (FD)- and CW-DOT (Continuous Wave-Diffuse Optical Tomography) method (a) overview and (b) example.

2.2. Simulation Overview

We performed simulations using diffusion theory [22,32] to evaluate the performance of the hybrid FD/CW DOI technique and compare it with the conventional topographic reflectance DOI. For the forward problem, the FEM numerical solver of the open source DOT software, NIRFAST [30,31], was used to generate tissue reflectance for tumor-containing breast tissue for the desired source–detector configuration. A modulation frequency of 200 MHz was used for FD data. Afterwards, random Gaussian noise of 1% complex amplitude and 1% reflectance was added to the simulated FD and CW data, respectively. We verified that this noise level is typical for our DOI imaging system, characterized from one-hour continuous measurements (121 iterations) of a homogeneous phantom of known optical properties. Finally, the tissue optical properties were recovered at each wavelength in the range of 650 to 1000 nm to simulate the hybrid DOI technique.

As our goal was to compare the hybrid DOI method to the conventional topographic DOI, we performed two different inversions. For the conventional topographic DOI method, a semi-infinite analytical diffusion model [33] that assumes optical homogeneity in the medium was utilized to extract 2D topographic maps of tissue optical properties (absorption μ_a and reduced scattering μ'_s) for each wavelength ranging from 650 to 1000 nm at every 5 nm. The optical properties corresponding to normal and tumor containing tissue were extracted at each wavelength by averaging the properties over regions of interest (ROIs) selected on the 2D maps. The tumor and normal ROI were manually chosen over the 2D spatial maps of reconstructed properties. These homogeneous model based results also served as the initial guess for the hybrid DOI hyperspectral recovery. Figure 2 depicts the simulation overview.

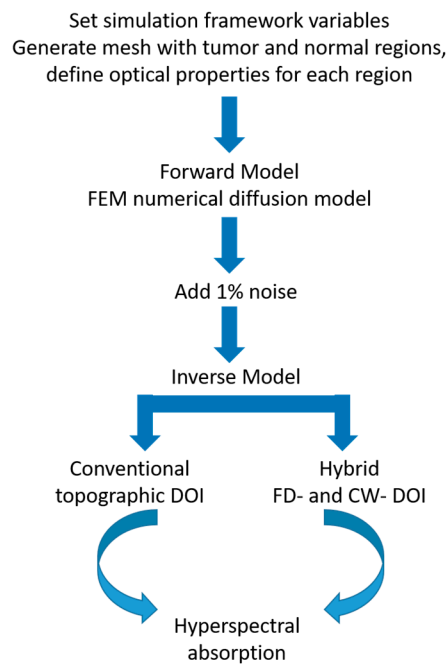


Figure 2. Simulation framework.

To generate simulated data, a 3D rectangular slab mesh consisting of 139,435 nodes corresponding to 710,944 tetrahedron elements was used. A second 3D slab mesh with a total of 45,688 nodes corresponding to 215,430 tetrahedron elements was generated to perform reconstructions to avoid inverse crime [34]. Our tissue model mimicked a human breast tissue containing an ellipsoidal tumor. The 20 mm × 30 mm × 20 mm ellipsoidal tumor was investigated at depths varying from 0 to 10 mm between the surface of the tissue (i.e., skin) and top surface of the tumor. This represents a typical range of palpable breast tumor depths studied with reflectance-based DOI [35]. The source and detector geometry represents the manual translation of a simple single source–detector separation (SDS) probe with a separation of 28 mm over a 1 cm spaced rectangular 2D grid pattern [5], similar to that used in the ACRIN 6691 multicenter trial of diffuse optical spectroscopy in breast cancer therapy [36]. We initially simulated an array of multiple SDSs, but because of use of hard spatial a priori information for normal and tumor regions within the heterogeneous tissue, the additional SDSs did not increase the overall accuracy. The overall geometry is illustrated in Figure 3. The source detector arrangement lies in such a way that the long axis of the ellipse was taken along the line between the source and detector. This was an arbitrary choice that is not expected to influence the simulations.

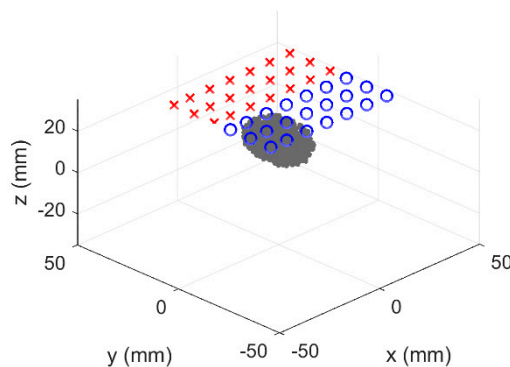


Figure 3. Simulated heterogeneous system. Blue circles and red crosses identify sources and detectors, respectively. The grey ellipsoid is the heterogeneity, which was varied in depth.

Table 1 lists the concentration of the absorbing components and scattering parameters specified in the heterogeneous tissue model. Optical properties were chosen based on chromophore concentrations (oxy-, deoxy-, water, and bulk lipids) and scattering parameters (a and b) of human breast tumors measured by DOT [37]. An additional absorption contribution has been added to the tumor containing tissue to model low-level absorption from unknown sources, and to demonstrate the lack of needing a spectral absorption constraint. For simplicity, the naphthol green B (NGB) dye spectrum was chosen because its absorption spectrum contains a single absorption feature in the desired spectral range.

Table 1. Normal versus tumor parameters used for simulations [37].

Parameters	Normal	Tumor
Absorbing Chromophores		
HbO (μM)	8.6	17.5
HHb (μM)	6.3	9.8
H ₂ O (%)	21.8	31.3
Lipids (%)	80.6	66.3
NGB (g/L)	–	0.05
Scattering Parameters		
Scattering amplitude (a) (mm^{-1})	2.29	3.11
Scattering power (b)	1.2	1.5

2.3. Tissue-Simulating Phantom Validation

The hybrid FD- and CW- DOT technique was evaluated on two inhomogeneous phantoms, where the inhomogeneities mimic a tumor mass in the breast. An additional absorbing dye has been exclusively added to the inclusion of the phantom, representing an a priori unknown tumor specific absorption.

2.3.1. Phantom Composition

Two heterogeneous phantoms, A and B, were constructed, both consisting of a 12.5 cm diameter cylindrical background material with a 2.6 cm diameter cylindrical inclusion in the center. The cylindrical inclusion is positioned in both phantoms such that the base of the inclusion is 2 mm from one side of the phantom. The base of the inclusion is 7 mm and 9 mm from the other end for phantoms A and B respectively. These exact depths were determined by the custom apparatus that was built to fabricate the heterogeneous phantoms, the mold, and the silicone volume poured. Figure 4 illustrates the geometry of the phantoms A and B in x-z plane.

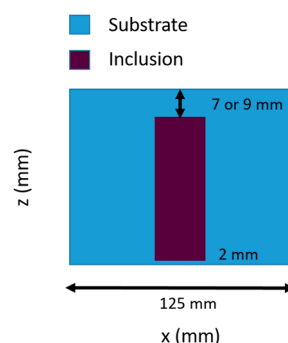


Figure 4. Heterogeneous phantom geometry in x-z plane.

Phantoms A and B were designed to have the same absorption contrast between the inclusion and the substrate. Phantom A was designed to show similar scattering, whereas Phantom B shows a scattering contrast between the inclusion and the substrate. This was done in order to test the ability of the hybrid DOI method to provide better scattering estimates to improve the CW reconstruction.

Both phantoms contained a P4 silicone rubber base and P4 silicone activator (Eager Polymers, Chicago, IL, USA). Anatase titanium (IV) oxide and water-soluble Nigrosin ink (Sigma-Aldrich, St. Louis, MO, USA) was added to the phantoms for scattering and absorption features [38]. The inclusion also contained NGB ink (Sigma-Aldrich, St. Louis, MO, USA) as an additional absorbing component.

2.3.2. Phantom Measurements

DOI measurements were captured with a custom-built system that combines discrete wavelength FD and broadband CW techniques [16]. Four laser diodes (660, 690, 785, and 830 nm) were sequentially swept from 50 to 500 MHz (each ~20 mW average power at the tissue) to acquire multifrequency amplitude and phase measurements using a 1 mm circular APD in contact with the phantom surface. For this study, only data at 200 MHz was used for reconstruction. The CW component of the DOI system consists of a tungsten-halogen white light source and a 1 mm core fiber coupled to the spectrometer to measure the reflectance spectra in the wavelength range of 650 to 1000 nm. More details of the imaging system have been provided elsewhere [39]. The DOI handheld imaging probe geometry, shown in Figure 5a, was used to make multiple measurements across the surface of the phantom with a source detector separation of 28 mm. Measurements are typically made by moving the probe in 1 cm increments along a rectangular grid coordinate system spanning the surface of the phantom. The dimensions of the rectangular grid pattern used were 7 cm \times 7 cm on both sides of the phantom. The grid size was chosen such that it fully encompasses the inclusion and captures the surrounding background composition. An example of the DOS (Diffuse Optical Spectroscopic) imaging grid locations on the phantom is shown in Figure 5b.

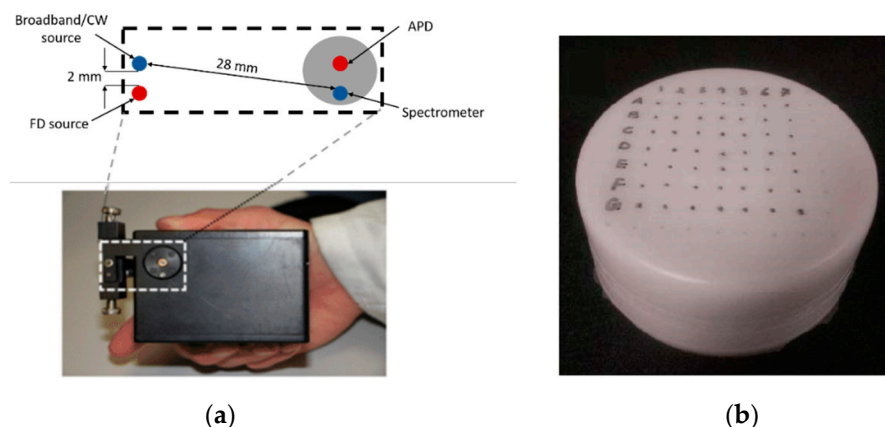


Figure 5. (a) DOS (Diffuse Optical Spectroscopic) handheld imaging probe geometry. (b) Rectangular grid measurement pattern on phantom (7 cm \times 7 cm).

3. Results

3.1. Simulated Results of Hybrid DOI Method

Each panel of Figure 6 shows a 2D cross section of the tumor-containing tissue in the Y-Z plane. Different columns correspond to different depths of the tumor simulated from the tissue surface (0, 5, and 10 mm), whereas different rows correspond to the ground truth μ_a and the simulated μ_a recovery at 650 nm.

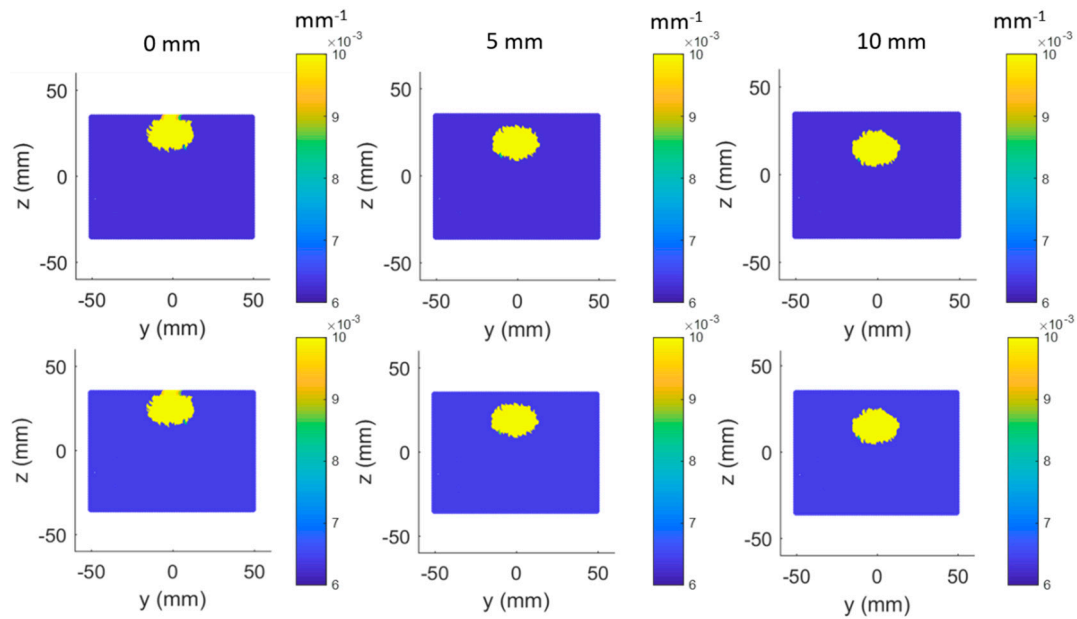


Figure 6. Ground truth (row 1) versus simulated recovery (row 2) in μ_a (650 nm) at different tumor depths (columns).

3.2. Simulated Results of Topographic DOI Method

The optical properties were recovered for every grid point measured using the homogenous model. Following this, the properties were spatially interpolated to generate 2D color maps from which ROIs were manually selected for the inclusion and substrate to quantify the properties for each wavelength. An example of the absorption map at 650 nm and the ROI selection is shown in Figure 7 below. The grid points have been overlaid on the figure.

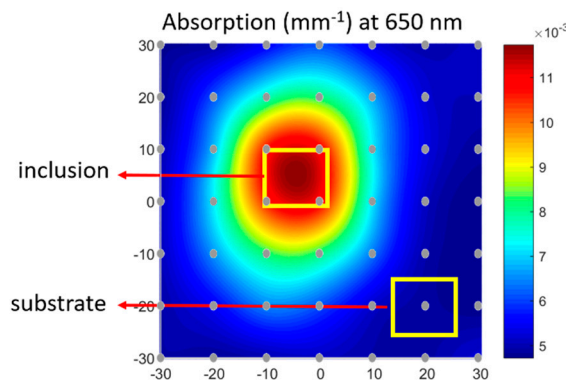


Figure 7. Spatially interpolated topographic DOI recovered absorption at 650 nm with region of interest (ROI) selection for tumor and normal regions.

Figure 8a,b shows a bar graph representation comparing the true values, hybrid DOI method recovery, and conventional topographic DOI recovery at a single wavelength (650 nm) for the multiple tumor depths (0–10 mm). The simulations were performed for five repetitions in order to observe the effects of the noise. The error bars represent the standard deviation in the recovered results over five repetitions. We investigated the variation in standard deviation up to 10 repetitions and considered five iterations to be a representative number required to estimate the variation in the results. Figure 8c,d shows the corresponding bar graph plots for μ'_s at 650 nm. The absolute differences and percentage differences of the hybrid DOI and conventional topographic DOI recovered μ_a and μ'_s from the true μ_a and μ'_s have been summarized in Table 2 for all tumor depths.

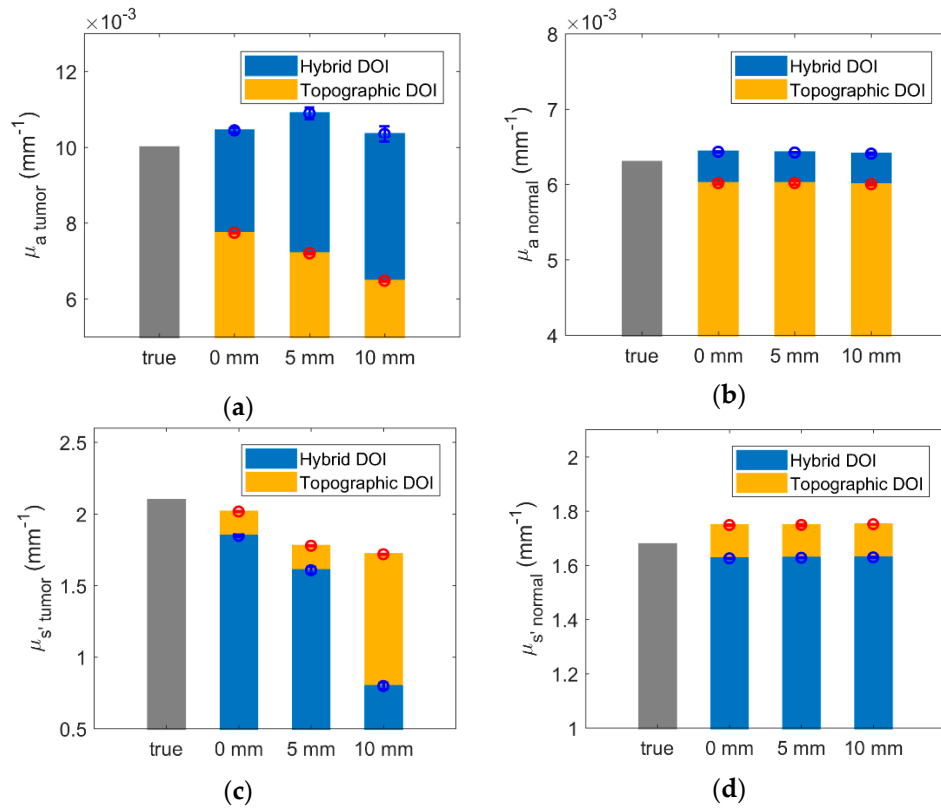


Figure 8. Bar plot representation of ground truth (gray), hybrid DOI, and conventional topographic DOI simulated recovery in μ_a at 650 nm for (a) tumor and (b) normal tissue and μ_s' at 650 nm for (c) tumor and (d) normal tissue.

Table 2. Difference and percent difference of recovered μ_a and μ_s' from true μ_a and μ_s' at 650 nm.

Depths (mm)	Tumor							
	Hybrid DOI				Topographic DOI			
	Difference from True (mm^{-1})		% Difference of mean from true (%)		Difference from True (mm^{-1})		% Difference of Mean from True (%)	
	μ_a	μ_s'	μ_a	μ_s'	μ_a	μ_s'	μ_a	μ_s'
0	$4.4 \times 10^{-4} \pm 6.3 \times 10^{-5}$	$-0.25 \pm 7.9 \times 10^{-3}$	4.4	-12.0	$-2.3 \times 10^{-3} \pm 1.6 \times 10^{-5}$	$-0.08 \pm 2.6 \times 10^{-3}$	-22.6	-3.9
5	$8.9 \times 10^{-4} \pm 1.5 \times 10^{-4}$	-0.49 ± 0.02	8.9	-23.5	$-2.8 \times 10^{-3} \pm 2.3 \times 10^{-5}$	$-0.32 \pm 2.4 \times 10^{-3}$	-28.0	-15.3
10	$3.5 \times 10^{-4} \pm 1.9 \times 10^{-4}$	-1.3 ± 0.02	3.5	-62.0	$-3.5 \times 10^{-3} \pm 2.1 \times 10^{-5}$	$-0.38 \pm 1.9 \times 10^{-3}$	-35.2	-18.2
	Normal							
	Hybrid DOI				Topographic DOI			
	Difference from true (mm^{-1})		% Difference of mean from true (%)		Difference from true (mm^{-1})		% Difference of mean from true (%)	
	μ_a	μ_s'	μ_a	μ_s'	μ_a	μ_s'	μ_a	μ_s'
0	$1.3 \times 10^{-4} \pm 5.7 \times 10^{-6}$	$-0.05 \pm 1.0 \times 10^{-3}$	2.1	-3.1	$-2.8 \times 10^{-4} \pm 1.6 \times 10^{-5}$	$0.07 \pm 2.3 \times 10^{-3}$	-4.5	4.2
5	$1.2 \times 10^{-4} \pm 3.5 \times 10^{-6}$	$-0.05 \pm 1.2 \times 10^{-3}$	1.9	-3.0	$-2.9 \times 10^{-4} \pm 2.2 \times 10^{-5}$	$0.07 \pm 3.5 \times 10^{-3}$	-4.5	4.3
10	$1.1 \times 10^{-4} \pm 1.2 \times 10^{-5}$	$-0.05 \pm 1.5 \times 10^{-3}$	1.7	-2.9	$-2.9 \times 10^{-4} \pm 1.1 \times 10^{-5}$	$0.07 \pm 1.1 \times 10^{-3}$	-4.7	4.4

The percentage difference of the hybrid DOI and topographic DOI recovered mean μ_a and μ_s' , from the true μ_a and μ_s' for the normal tissue is below 5% for all tumor depths considered. The percent difference of topographic DOI recovered tumor (μ_a and μ_s') values increases from 22.6% and 3.9%, to 35.2% and 18.2%, respectively, with increasing tumor depths from 0 mm to 10 mm. This is because conventional DOI topography technique assumes optical homogeneity. As the tumor depth increases, the detected light probes lesser volume of the tumor, resulting in more dilution in the recovered tumor/inhomogeneity absorption spectra. The hybrid DOI reconstructed tumor absorption demonstrates more consistency over varying tumor depths with a percentage difference of (−4.4%) versus (−3.5%) for tumor depth of 0 mm versus 10 mm. This is because the partial volume artifacts do not affect tomographic reconstructions as severely. However, the percent difference of hybrid DOI recovered tumor μ_s' values increases from 12% to 62% with increasing tumor depths from 0 mm to 10 mm.

The recovered broadband optical properties μ_a and μ_s' using the hybrid DOI technique for wavelength range of 650 to 1000 nm are shown in Figures 9 and 10, respectively. Each panel of Figures 9 and 10 compares the hyperspectral results from hybrid DOI technique to the topographic DOI results and the true (μ_a, μ_s') values. Different columns correspond to different depths of the tumor from the tissue surface (0, 5, and 10 mm), whereas different rows correspond to the normal and tumor containing tissue optical properties.

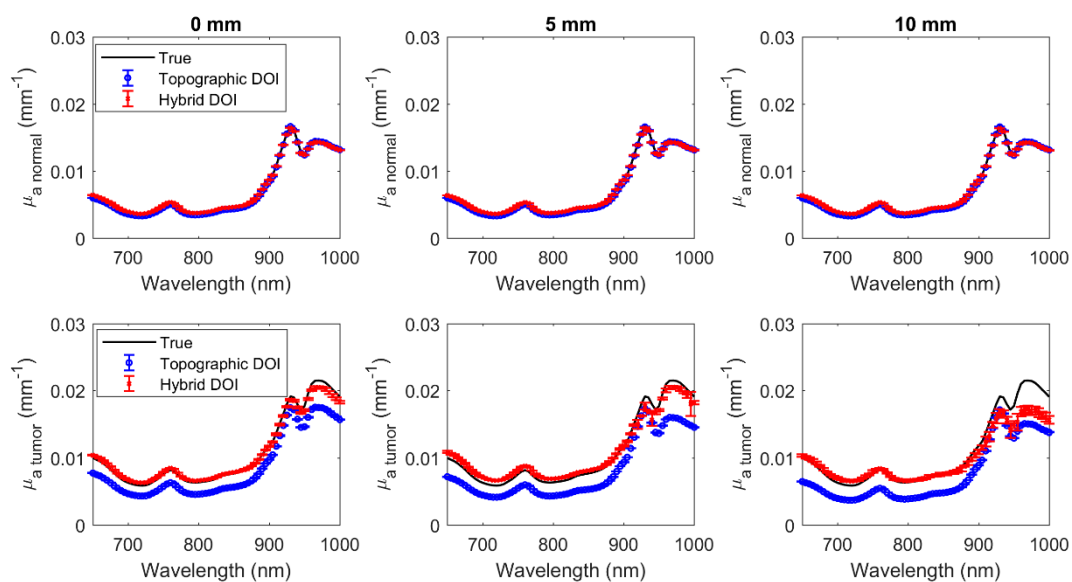


Figure 9. Hyperspectral normal (row 1) and tumor μ_a (row 2) at wavelengths 650 nm to 1000 nm at different tumor depths (columns).

Reconstructions were acquired for 71 wavelengths ranging from 650 to 1000 nm every 5 nm (Figures 9 and 10). The error bars indicate the deviation over five repetitions. The mean difference and the mean percentage difference of the recovered (μ_a, μ_s') from the true (μ_a, μ_s') over all wavelengths have been summarized in Table 3 for both topographic DOI and hybrid DOI techniques at all tumor depths considered.

Hybrid DOI and topographic DOI techniques recover the hyperspectral optical properties (μ_a, μ_s') for the normal tissue with a maximum mean percentage difference of 1.64% and 1.9%, and 4.10% and 3.37%, respectively, over 71 wavelengths in the range of 650 to 1000 nm over all tumor depths. Broadband μ_a recovery of the tumor is also more accurate for the hybrid DOI technique with a mean percent difference less than 10% versus the conventional topographic DOI with a mean percent difference greater than 20% for all the tumor depths considered. However, the mean percent difference of the hybrid DOI and conventional DOI reconstructed μ_s' deteriorates from 7.86% and 22.35% to 47.86% and 32.26% for a tumor depth of 0 mm versus 10 mm. Simulations show that hybrid DOI is

expected to be at least ~10x more accurate at recovering the tumor absorption than conventional single SDS DOI topography, however it is less sensitive to scattering differences in deeper tumors.

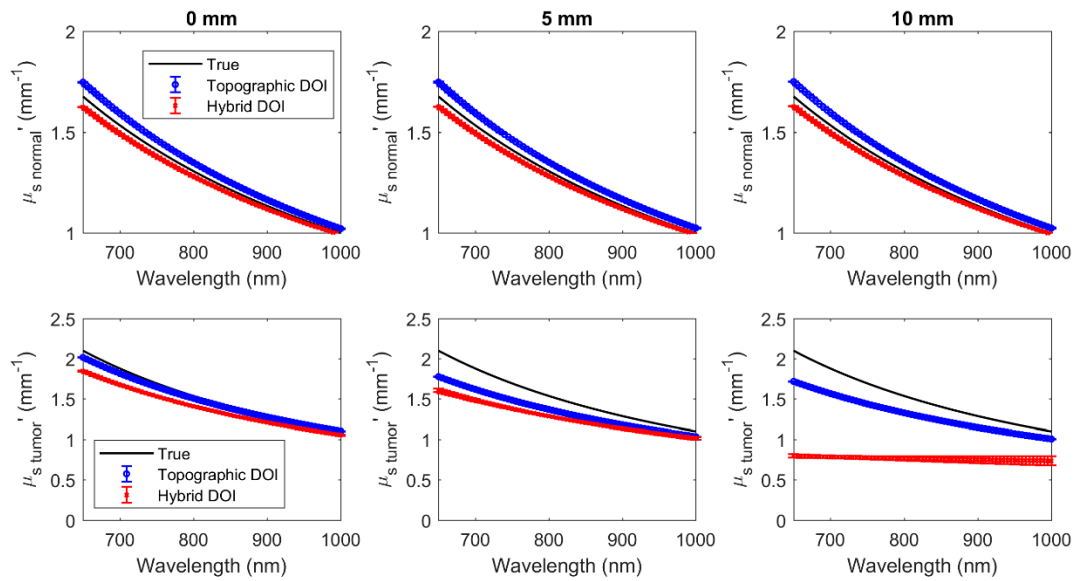


Figure 10. Hyperspectral normal (row 1) and tumor μ_{s}' (row 2) at wavelengths 650 nm to 1000 nm at different tumor depths (columns).

Table 3. Mean difference and mean percentage difference of recovered (μ_a, μ_{s}') from true (μ_a, μ_{s}') over all wavelengths.

Depths (mm)	Tumor							
	Hybrid DOI				Topographic DOI			
	Mean Difference from True Over all Wavelengths (mm ⁻¹)		Mean% Change from True Over all Wavelengths (%)		Mean Difference from True Over all Wavelengths (mm ⁻¹)		Mean% Change from True Over all Wavelengths (%)	
	μ_a	μ_{s}'	μ_a	μ_{s}'	μ_a	μ_{s}'	μ_a	μ_{s}'
0	3.9×10^{-4}	0.13	3.87	7.86	2.2×10^{-3}	0.03	22.35	1.78
5	7.2×10^{-4}	0.25	7.49	15.34	2.6×10^{-3}	0.16	26.52	10.38
10	1.2×10^{-3}	0.75	8.39	47.86	3.2×10^{-3}	0.21	32.26	13.04
	Normal							
	Hybrid DOI				Topographic DOI			
	Mean difference from true over all wavelengths (mm ⁻¹)		Mean% change from true over all wavelengths (%)		Mean difference from true over all wavelengths (mm ⁻¹)		Mean% change from true over all wavelengths (%)	
	μ_a	μ_{s}'	μ_a	μ_{s}'	μ_a	μ_{s}'	μ_a	μ_{s}'
0	1.1×10^{-4}	0.03	1.64	1.9	1.9×10^{-4}	0.04	3.65	3.14
5	1.0×10^{-4}	0.02	1.50	1.76	2.1×10^{-4}	0.04	3.89	3.30
10	1.0×10^{-4}	0.02	1.35	1.64	2.2×10^{-4}	0.04	4.10	3.37

3.3. Phantom Experimental Results

Figures 11 and 12 show the broadband μ_a and μ_{s}' spectra of the inclusion and substrate optical properties reconstructed from the two heterogeneous tissue-simulating phantoms. Each panel of Figures 11 and 12 compares the broadband results from hybrid DOI technique to the topographic DOI results and the true (μ_a, μ_{s}') values of the phantom. Broadband optical properties for substrate

and inclusion were reconstructed for 71 wavelengths from 650 to 1000 nm on each side of phantoms A and B. Measurements on different sides of the phantoms corresponds to different depths of the inclusion from the phantom surface. The top and bottom row correspond to the substrate and inclusion absorption of the phantoms, respectively. The true spectra for the substrate was measured on the inclusion phantoms (A and B), by acquiring a measurement away from the inclusion. This was done to ensure that the optical path does not interrogate the inclusion. The true spectra for the inclusions of phantoms A and B were acquired by measuring a separate homogenous phantoms that were made from the same batch material/composition of the inclusions in A and B.

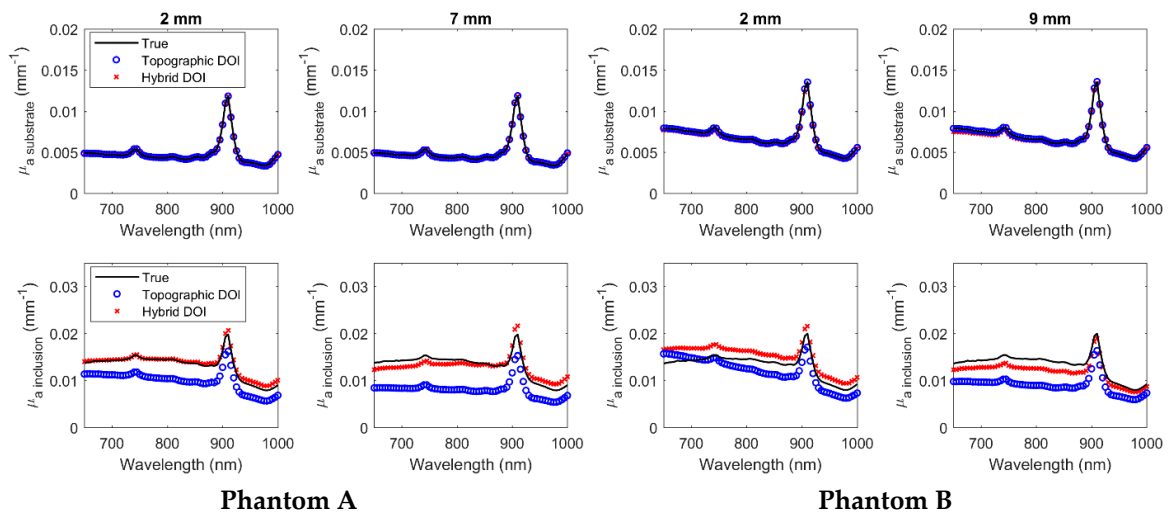


Figure 11. Hyperspectral substrate (row 1) and inclusion μ_a (row 2) at wavelengths 650 nm to 1000 nm for phantoms A and B.

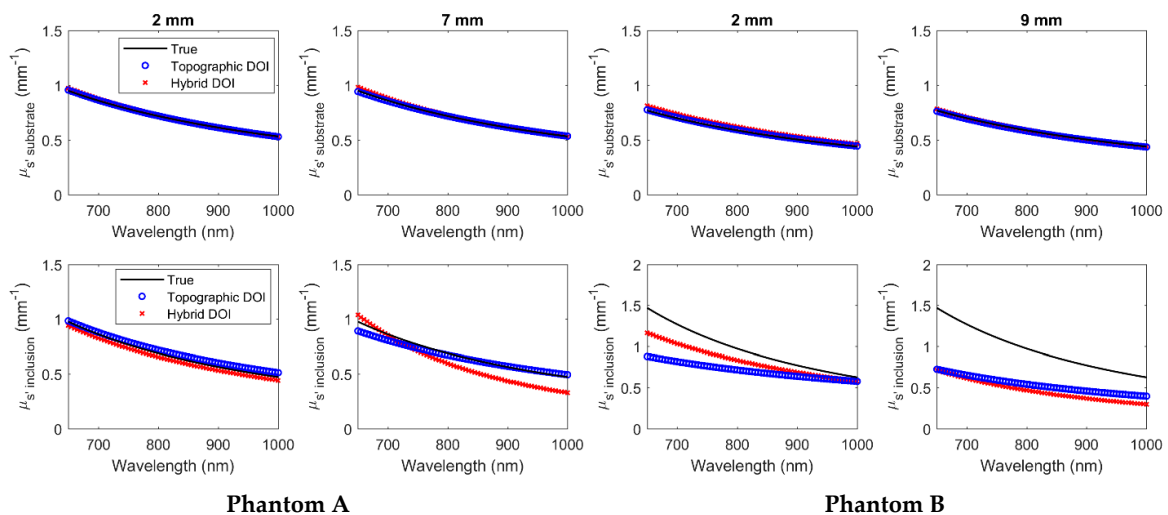


Figure 12. Hyperspectral substrate (row 1) and inclusion μ_s' (row 2) at wavelengths 650 nm to 1000 nm for phantoms A and B.

The mean difference and mean percentage change of the (μ_a, μ_s') recovered from the true (μ_a, μ_s') over all wavelengths have been summarized in Tables 4 and 5, respectively, for phantoms A and B using both hybrid DOI and conventional topographic DOI techniques.

Table 4. Mean difference and mean percentage change of recovered (μ_a, μ_s') from true (μ_a, μ_s') over all wavelengths for phantom A.

Depths (mm)	Phantom A—Inclusion							
	Hybrid DOI				Topographic DOI			
	Mean Difference from True Over all Wavelengths (mm^{-1})		Mean% Change from True Over all Wavelengths (%)		Mean Difference from True Over all Wavelengths (mm^{-1})		Mean% Change from True Over all Wavelengths (%)	
	μ_a	μ_s'	μ_a	μ_s'	μ_a	μ_s'	μ_a	μ_s'
2	4.0×10^{-4}	0.03	3.65	4.99	3.3×10^{-3}	0.03	25.19	4.89
7	1.0×10^{-3}	0.09	8.37	15.34	5.1×10^{-3}	0.03	38.43	3.52
Depths (mm)	Phantom A—Substrate							
	Hybrid DOI				Topographic DOI			
	Mean difference from true over all wavelengths (mm^{-1})		Mean% change from true over all wavelengths (%)		Mean difference from true over all wavelengths (mm^{-1})		Mean% change from true over all wavelengths (%)	
	μ_a	μ_s'	μ_a	μ_s'	μ_a	μ_s'	μ_a	μ_s'
2	4.6×10^{-5}	0.008	1.01	0.78	3.31×10^{-5}	0.0018	0.75	0.32
7	8.1×10^{-5}	0.010	1.78	1.32	3.32×10^{-5}	0.002	0.76	0.31

Table 5. Mean difference and mean percentage change of recovered (μ_a, μ_s') from true (μ_a, μ_s') over all wavelengths for phantom B.

Depths (mm)	Phantom B—Inclusion							
	Hybrid DOI				Topographic DOI			
	Mean Difference from True Over all Wavelengths (mm^{-1})		Mean% Change from True over All Wavelengths (%)		Mean Difference from True Over all Wavelengths (mm^{-1})		Mean% Change from True over All Wavelengths (%)	
	μ_a	μ_s'	μ_a	μ_s'	μ_a	μ_s'	μ_a	μ_s'
2	1.8×10^{-3}	0.14	13.89	13.67	1.8×10^{-3}	0.25	13.88	24.12
9	1.5×10^{-3}	0.49	10.64	51.99	4.3×10^{-3}	0.43	32.05	43.49
Depths (mm)	Phantom B—Substrate							
	Hybrid DOI				Topographic DOI			
	Mean difference from true over all wavelengths (mm^{-1})		Mean% change from true over all wavelengths (%)		Mean difference from true over all wavelengths (mm^{-1})		Mean% change from true over all wavelengths (%)	
	μ_a	μ_s'	μ_a	μ_s'	μ_a	μ_s'	μ_a	μ_s'
2	1.8×10^{-4}	0.03	2.62	5.58	1.7×10^{-5}	0.005	0.22	0.90
9	1.9×10^{-4}	0.004	2.64	0.67	1.66×10^{-5}	0.0052	0.23	0.91

As shown in Figures 11 and 12 and Tables 4 and 5, both hybrid DOI and topographic DOI techniques recover the broadband optical properties (μ_a, μ_s') for the phantom substrate with a low mean percentage difference less than 6% from true values over all wavelengths in all measured scenarios. This trend in the experimental agrees with the simulated scenarios in Table 3, where the hybrid DOI technique recovered broadband normal optical properties with a mean accuracy of less than 5% over all 71 wavelengths.

For the broadband μ_a recovery of the inclusion spectra in the phantoms, the hybrid DOI technique demonstrates a lower mean percent difference from true μ_a versus the conventional topographic DOI for both shallow and deep ends of phantoms A and B. Therefore, the experimental results also agree with the simulated trends by demonstrating a mean accuracy over all wavelengths for optical

absorption of 8.37% versus 38.43% and 10.64% versus 32.05% for hybrid DOI versus topographic DOI methods at deep ends of phantom A and B, respectively. Similar to simulated μ_s' results (Table 3), the phantom experimental results also demonstrate a poorer accuracy in the scattering estimation with 15.34% versus 3.52% and 51.99% versus 43.49% for hybrid DOI versus topographic DOI methods at deep ends of phantom A and B, respectively. Overall, the hybrid DOI accuracy in the simulated results agrees well with the phantom experimental results (Table 3 versus Tables 4 and 5).

4. Discussion

In this study, a hybrid DOI method is presented that combines discrete wavelength FD and broadband CW reflectance measurements for quantitative measurements of the optical properties of deep tissue inclusions with a simple reflectance-based handheld probe configuration. Simulations showed that the new hybrid DOI method demonstrates enhanced accuracy with a relatively low mean percentage difference from true values in μ_a reconstructions over the conventional topographic DOI technique for both normal and tumor-containing tissue at all tumor depths considered. This showed that partial volume artifacts, unlike the homogeneous model reconstructions employed by the conventional method, were corrected by the hybrid DOI method. The hybrid DOI technique also demonstrated accuracy and repeatability in recovering hyperspectral absorption on the two heterogeneous phantoms A and B at varying inclusion depths in Figure 11.

The hybrid DOI results for deep inhomogeneities (such as 10 mm) show large error bars at wavelengths above 900 nm compared to the conventional topographic DOI results (Figures 9 and 10). This is because in topographic DOI, a homogeneous model is employed where all photons measured at the tissue surface are considered to estimate optical properties for the homogeneous medium. However, in the hybrid technique, optical properties are estimated for tumor and normal regions separately. To estimate the optical properties of the inhomogeneity, the hybrid technique requires photons measured at the surface that have traversed the optical inhomogeneity/tumor (>10 mm). Therefore, for deeper inclusions (such as 10 mm), the light measured that have traversed the inhomogeneity/inclusion is limited, thereby resulting in more variation over repetitions.

However, the simulations and the phantom experimental results show that the hybrid DOI technique demonstrates at poor scattering recovery for deeper inhomogeneities. The hybrid DOI technique recovered broadband μ_s' with a mean percent difference of ~48% and ~52% over all wavelengths for the 10 mm tumor depth simulation and the deep end of Phantom B (predicted inclusion depth 9 mm), respectively. As expected, accuracy is reduced when attempting to characterize deeper inhomogeneities. Indeed, the poor scattering recovery of the deep lesions compared to the conventional topographic technique was unexpected. We have investigated the amplitude and phase sensitivity with respect to absorption and scattering for increasing tumor depths from 0 to 10 mm, and it was observed that the overall sensitivity of amplitude and phase to scattering is considerably lower compared to the sensitivity to absorption. In addition, the sensitivity of amplitude to scattering was observed to decrease drastically when the tumor depth increases from 5 mm to 10 mm. Therefore, we can conclude that the scattering differences are not as perceptible as the absorption in deeper inclusions. However, FD component can still be considered significant in deeper, as it estimates a good scattering for the background/normal tissue. As part of our future work, we will perform more simulations to study this effect, but we hypothesize that this is due to reduced signal to noise ratio because of the increased optical attenuation in deeper tumors.

Reflectance-based handheld probes have the advantage of being fast and portable, can be applied to a wide range of imaging applications, and used in a variety of clinical settings. We have investigated the ability to recover the broadband optical properties of a buried tumor-like inclusion using measurements captured with a single SDS probe translated in grid pattern. Besides representing a straightforward case for our analysis, this probe configuration was the same used in the ACRIN 6691 multicenter clinical trial of diffuse optical spectroscopy in breast cancer therapy. We confirmed our hypothesis that applying the hybrid DOI technique could greatly improve the accuracy of tumor characterization

compared to the homogeneous topographic approach used in ACRIN 6691 and related studies [36]. This would be helpful, for example, in better resolving optical property differences in highly attenuating tissue regions such as characterizing breast masses in the areola. Therefore, in this study, our goal was to compare the accuracy of the hybrid DOI technique to the traditional topographic approach when applied to the same raw diffuse optical dataset.

Topographic DOI does not consider any depth-dependent variations in the tissue composition and assumes optical homogeneity, which contributes to significant errors in optical property estimation of tissue inhomogeneities. On the contrary, the hybrid technique considers tissue inhomogeneities by reconstructing optical properties for different regions (normal and tumor) within the tissue. This additional spatial information is intended to be provided by complementary medical imaging, such as a ultrasound which has been integrated with reflectance-based DOI probes [40,41]. Indeed, these studies have described how spatial guided techniques, such as ultrasound-guided DOT, help improve lesion localization and light quantification accuracy, which leads to more accurate estimation of hemoglobin content in breast lesions. Our method differs from these by providing access to much more optical contrast and chromophore accuracy through broadband optical property reconstruction. Though this study is not able to assess the clinical utility of this additional contrast and accuracy, we hypothesize that it would be beneficial in applications where accurate quantitative assessment of tissue optical properties is critical, such as in noninvasive diagnosis of human malignancies including breast, colorectal, and thyroid tumors. Furthermore, our technique is sensitive to absorption contributions from a priori unknown chromophores, which has been shown to be useful for different diagnosis of breast lesions [9–13].

Prior studies have also reported the measurement of broadband optical absorption over as many as 120 wavelengths using CW-only DOT measurements [42]. However, these studies assume that the tissue scattering coefficient is known, because the CW method alone has limited capability to separate absorption from scattering in the DOT reconstruction [25,43]. This emphasizes the significance of the FD component in the hybrid DOI technique as it allows us to obtain good estimates of scattering across the entire wavelength range. The simulation and experimental results demonstrates that adding the FD component provides accurate absorption estimation for normal tissue and relatively shallow tumors. In addition, for deeper inhomogeneities (9 and 10 mm), a good scattering estimate of the normal tissue is significant to acquire accurate absorption estimates of the tumor.

In this hybrid DOI approach, broadband optical properties are recovered at each wavelength individually without a priori spectral constraints, but with spatial constraints to reduce computational complexity and time. Use of prior information for reconstructions can be categorized as hard priors and soft priors [31]. Soft prior information has been extensively used in a number of experimental and clinical settings and has been found to be more robust in the presence of uncertainty in prior information [44,45]. A limitation of our approach is requiring hard priors for the reconstructions wherein bulk homogeneous values are reconstructed for each region specified. We have restricted the hard prior reconstructions to two regions, namely, normal and tumor containing tissue. However, the same technique can also be extended to multiple regions, such as in cases of multiple lesions or to model heterogeneity within the tumor itself. The advantage of hard prior reconstructions is that the total number of unknowns are reduced dramatically, thereby making the problem better posed and immensely reducing the computational complexity [31]. However, a drawback is that the spatial resolution is now limited by the size of the defined regions and its accuracy is highly dependent on the quality of the a priori information. The dependency on the uncertainty of the lesion location from the tissue surface can be addressed by modifying the objective function to also reconstruct spatial parameters such as the size and depth of the lesion or the gradient between the inclusion and background. Another limitation of a priori spatial constraints is that it assumes optical and structural contrast are perfectly colocalized, which is likely not true in complex biological tissues. Furthermore, we have modeled an ellipsoidal inclusion to represent a lesion containing tissue. However, the shape

of the lesion does not have to be ellipsoidal and we can apply any arbitrary shape of the inhomogeneity to the hybrid DOI problem.

In summary, this new hybrid DOI method is promising for improving broadband characterization of deep tissue inhomogeneities using a simple reflectance-based probe. Our future work includes studying the effect of optical attenuation in deeper tumors and attempting to improve reconstruction of deeper inhomogeneities by providing the hybrid method an advantage of viewing multiple transverse views of the tissue at each grid point. We also intend to study the influence of noise model and depth uncertainty of phantom inclusions in the mismatch of simulated and experimental result accuracy. We are also applying the hybrid DOI method to characterize human breast lesions and evaluate the clinical utility of the enhanced optical information.

Author Contributions: S.V. executed the simulations, performed the experiments, analyzed the data, and wrote the paper; F.F. provided ideas and directions, analyzed the data, and reviewed the manuscript; C.C. designed and fabricated the tissue-simulating phantoms; S.B. fabricated the tissue-simulating phantoms; T.D.O. conceptualized the idea, supervised the entire work, analyzed the data, and reviewed and edited the manuscript. All authors have read and agreed to the published version of the manuscript.

Funding: This research was funded by the American Cancer Society, Pilot Project Grant from Institutional Research Grant number IRG-14-195-01.

Conflicts of Interest: The authors declare no conflicts of interest.

References

- O'Sullivan, T.; Cerussi, A.E.; Cuccia, D.J.; Tromberg, B.J. Diffuse optical imaging using spatially and temporally modulated light. *J. Biomed. Opt.* **2012**, *17*, 0713111. [[CrossRef](#)]
- Cerussi, A.E.; Shah, N.S.; Hsiang, D.; Durkin, A.; Butler, J.A.; Tromberg, B.J. In vivo absorption, scattering, and physiologic properties of 58 malignant breast tumors determined by broadband diffuse optical spectroscopy. *J. Biomed. Opt.* **2006**, *11*, 044005. [[CrossRef](#)] [[PubMed](#)]
- Cerussi, A.E.; Hsiang, D.; Shah, N.; Mehta, R.; Durkin, A.; Butler, J.; Tromberg, B.J. Predicting response to breast cancer neoadjuvant chemotherapy using diffuse optical spectroscopy. *Proc. Natl. Acad. Sci. USA* **2007**, *104*, 4014–4019. [[CrossRef](#)] [[PubMed](#)]
- Zhu, Q.; Kurtzman, S.H.; Hegde, P.; Tannenbaum, S.; Kane, M.; Huang, M.; Chen, N.; Jagjivan, B.; Zarfos, K. Utilizing Optical Tomography with Ultrasound Localization to Image Heterogeneous Hemoglobin Distribution in Large Breast Cancers. *Neoplasia* **2005**, *7*, 263–270. [[CrossRef](#)] [[PubMed](#)]
- O'Sullivan, T.; Leproux, A.; Chen, J.H.; Bahri, S.; Matlock, A.; Roblyer, D.M.; McLaren, C.E.; Chen, W.-P.; Cerussi, A.E.; Su, M.; et al. Optical imaging correlates with magnetic resonance imaging breast density and reveals composition changes during neoadjuvant chemotherapy. *Breast Cancer Res.* **2013**, *15*, R14. [[CrossRef](#)]
- Shah, N.; Cerussi, A.E.; Jakubowski, D.B.; Hsiang, D.; Butler, J.A.; Tromberg, B.J. Spatial variations in optical and physiological properties of healthy breast tissue. *J. Biomed. Opt.* **2004**, *9*, 534–541. [[CrossRef](#)]
- Choe, R.; Corlu, A.; Lee, K.; Durduran, T.; Konecky, S.D.; Grosicka-Koptyra, M.; Arridge, S.R.; Czerniecki, B.J.; Fraker, D.L.; DeMichele, A.; et al. Diffuse Optical Tomography of Breast Cancer during Neoadjuvant Chemotherapy: A Case Study with Comparison to MRI. *Med. Phys.* **2005**, *32*, 1128–1139. [[CrossRef](#)]
- Shah, N.; Gibbs, J.; Wolverton, D.; Cerussi, A.; Hylton, N.; Tromberg, B.J. Combined diffuse optical spectroscopy and contrast-enhanced magnetic resonance imaging for monitoring breast cancer neoadjuvant chemotherapy: A case study. *J. Biomed. Opt.* **2005**, *10*, 051503. [[CrossRef](#)]
- Kukreti, S.; Cerussi, A.; Tromberg, B.; Gratton, E. Intrinsic tumor biomarkers revealed by novel double-differential spectroscopic analysis of near-infrared spectra. *J. Biomed. Opt.* **2007**, *12*, 20509. [[CrossRef](#)]
- Kukreti, S.; Cerussi, A.; Tromberg, B.; Gratton, E. Intrinsic near-infrared spectroscopic markers of breast tumors. *Dis. Markers* **2008**, *25*, 281–290. [[CrossRef](#)]
- Kukreti, S.; Cerussi, A.E.; Tanamai, W.; Hsiang, D.; Tromberg, B.J.; Gratton, E. Characterization of metabolic differences between benign and malignant tumors: High-spectral-resolution diffuse optical spectroscopy. *Radiology* **2010**, *254*, 277–284. [[CrossRef](#)]

12. Leproux, A.; Durkin, A.F.; Compton, M.; Cerussi, A.E.; Gratton, E.; Tromberg, B.J. Assessing tumor contrast in radiographically dense breast tissue using Diffuse Optical Spectroscopic Imaging (DOSI). *Breast Cancer Res.* **2013**, *15*, R89. [[CrossRef](#)]
13. Leproux, A.; Kim, Y.M.; Min, J.W.; McLaren, C.E.; Chen, W.-P.; O'Sullivan, T.; Lee, S.-H.; Chung, P.-S.; Tromberg, B.J. Differential diagnosis of breast masses in South Korean premenopausal women using diffuse optical spectroscopic imaging. *J. Biomed. Opt.* **2016**, *21*, 74001. [[CrossRef](#)] [[PubMed](#)]
14. Tromberg, B.J.; Pogue, B.W.; Paulsen, K.D.; Yodh, A.G.; Boas, D.A.; Cerussi, A.E. Assessing the future of diffuse optical imaging technologies for breast cancer management. *Med. Phys.* **2008**, *35*, 2443–2451. [[CrossRef](#)]
15. Hull, E.L.; Nichols, M.; Foster, T.H. Quantitative broadband near-infrared spectroscopy of tissue-simulating phantoms containing erythrocytes. *Phys. Med. Boil.* **1998**, *43*, 3381–3404. [[CrossRef](#)] [[PubMed](#)]
16. Bevilacqua, F.; Berger, A.J.; Cerussi, A.E.; Jakubowski, D.; Tromberg, B.J. Broadband absorption spectroscopy in turbid media by combined frequency-domain and steady-state methods. *Appl. Opt.* **2000**, *39*, 6498–6507. [[CrossRef](#)] [[PubMed](#)]
17. Sekar, S.K.V.; Mora, A.D.; Bargigia, I.; Martinenghi, E.; Lindner, C.; Farzam, P.; Pagliuzzi, M.; Durduran, T.; Taroni, P.; Pifferi, A.; et al. Broadband (600–1350 nm) Time-Resolved Diffuse Optical Spectrometer for Clinical Use. *IEEE J. Sel. Top. Quantum Electron.* **2015**, *22*, 406–414. [[CrossRef](#)]
18. Tachtsidis, I.; Leung, T.S.; Tahir, B.; Elwell, C.; Kohl-Bareis, M.; Gramer, M.; Cooper, C. A Hybrid Multi-Distance Phase and Broadband Spatially Resolved Algorithm for Resolving Absolute Concentrations of Chromophores in the Near-Infrared Light Spectrum: Results from Studies in Dynamic Phantoms. *Adv. Exp. Med. Biol.* **2010**, *662*, 169–175, Published online 2010.
19. Tachtsidis, I.; Gao, L.; Leung, T.S.; Kohl-Bareis, M.; Cooper, C.; Elwell, C. A Hybrid Multi-Distance Phase and Broadband Spatially Resolved Spectrometer and Algorithm for Resolving Absolute Concentrations of Chromophores in the Near-Infrared Light Spectrum. In *Single Molecule and Single Cell Sequencing*; Springer Science and Business Media LLC: Berlin/Heidelberg, Germany, 2010; Volume 662, pp. 169–175.
20. Kitsmiller, V.; Dummer, M.; Johnson, K.; O'Sullivan, T. Tunable vertical cavity surface emitting lasers for use in the near infrared biological window. *Proc. SPIE* 10488, Optical Fibers and Sensors for Medical Diagnostics and Treatment Applications XVIII. Available online: <https://www.spiedigitallibrary.org/conference-proceedings-of-spie/10488/104880L/Tunable-vertical-cavity-surface-emitting-lasers-for-use-in-the/10.1117/12.2290899.short> (accessed on 13 February 2018).
21. Boas, D.A.; Dale, A.M.; Franceschini, M.A. Diffuse optical imaging of brain activation: Approaches to optimizing image sensitivity, resolution, and accuracy. *NeuroImage* **2004**, *23*, S275–S288. [[CrossRef](#)]
22. Bigio, I.J.; Fantini, S. *Quantitative Biomedical Optics: Theory, Methods, and Applications*; Cambridge University Press: Cambridge, UK, 2016.
23. Wang, J.; Davis, S.C.; Srinivasan, S.; Jiang, S.; Pogue, B.W.; Paulsen, K.D. Spectral tomography with diffuse near-infrared light: Inclusion of broadband frequency domain spectral data. *J. Biomed. Opt.* **2008**, *13*, 041305. [[CrossRef](#)]
24. Culver, J.P.; Choe, R.; Holboke, M.J.; Zubkov, L.; Durduran, T.; Slemper, A.; Ntziachristos, V.; Chance, B.; Yodh, A.G. Three-dimensional diffuse optical tomography in the parallel plane transmission geometry: Evaluation of a hybrid frequency domain/continuous wave clinical system for breast imaging. *Med. Phys.* **2003**, *30*, 235–247. [[CrossRef](#)] [[PubMed](#)]
25. Corlu, A.; Choe, R.; Durduran, T.; Lee, K.; Schweiger, M.; Arridge, S.; Hillman, E.M.C.; Yodh, A.G. Diffuse optical tomography with spectral constraints and wavelength optimization. *Appl. Opt.* **2005**, *44*, 2082–2093. [[CrossRef](#)] [[PubMed](#)]
26. Kitsmiller, V.J.; O'Sullivan, T.; Stillwell, R.A. Toward handheld real time frequency domain diffuse optical spectroscopy. *Proc. SPIE* 10874, Optical Tomography and Spectroscopy of Tissue XIII, 1087405. Available online: <https://www.spiedigitallibrary.org/conference-proceedings-of-spie/10874/1087405/Toward-handheld-real-time-frequency-domain-diffuse-optical-spectroscopy/10.1117/12.2508911.full> (accessed on 1 March 2019).
27. Chen, N.G.; Guo, P.; Yan, S.; Piao, D.; Zhu, Q. Simultaneous near-infrared diffusive light and ultrasound imaging. *Appl. Opt.* **2001**, *40*, 6367–6380. [[CrossRef](#)] [[PubMed](#)]

28. Wang, X.; Pogue, B.W.; Jiang, S.; Dehghani, H.; Song, X.; Srinivasan, S.; Brooksby, B.A.; Paulsen, K.D.; Kogel, C.; Poplack, S.P.; et al. Image reconstruction of effective Mie scattering parameters of breast tissue in vivo with near-infrared tomography. *J. Biomed. Opt.* **2006**, *11*, 041106. [[CrossRef](#)]
29. Jacques, S.L. Optical properties of biological tissues: A review. *Phys. Med. Boil.* **2013**, *58*, R37–R61. [[CrossRef](#)]
30. Dehghani, H.; Eames, M.E.; Yalavarthy, P.; Davis, S.C.; Srinivasan, S.; Carpenter, C.M.; Pogue, B.W.; Paulsen, K.D. Near Infrared Optical Tomography Using NIRFAST: Algorithm for Numerical Model and Image Reconstruction. *Commun. Numer. Methods Eng.* **2008**, *25*, 711–732. [[CrossRef](#)]
31. Dehghani, H.; Srinivasan, S.; Pogue, B.W.; Gibson, A. Numerical Modelling and Image Reconstruction in Diffuse Optical Tomography. *Philos. Trans. A Math. Phys. Eng. Sci.* **2009**, *367*, 3073–3093. [[CrossRef](#)]
32. Haskell, R.C.; Svaasand, L.O.; Tsay, T.-T.; Feng, T.-C.; McAdams, M.S.; Tromberg, B.J. Boundary conditions for the diffusion equation in radiative transfer. *J. Opt. Soc. Am. A* **1994**, *11*, 2727. [[CrossRef](#)]
33. Cerussi, A.; Tromberg, B. Photon Migration Spectroscopy Frequency- Domain Techniques. In *Biomedical Photonics Handbook*; CRC Press: Boca Raton, FL, USA, 2003.
34. Lionheart, W. EIT reconstruction algorithms: Pitfalls, challenges and recent developments. *Physiol. Meas.* **2004**, *25*, 125–142. [[CrossRef](#)]
35. Ueda, S.; Yoshizawa, N.; Shigekawa, T.; Takeuchi, H.; Ogura, H.; Osaki, A.; Saeki, T.; Ueda, Y.; Yamane, T.; Kuji ISakahara, H. Near-Infrared Diffuse Optical Imaging for Early Prediction of Breast Cancer Response to Neoadjuvant Chemotherapy: A Comparative Study Using 18F-FDG PET/CT. *J. Nucl. Med.* **2016**, *57*, 1189–1195. [[CrossRef](#)]
36. Tromberg, B.J.; Zhang, Z.; Leproux, A.; O’Sullivan, T.; Cerussi, A.E.; Carpenter, P.M.; Mehta, R.; Roblyer, D.M.; Yang, W.; Paulsen, K.D.; et al. Predicting Responses to Neoadjuvant Chemotherapy in Breast Cancer: ACRIN 6691 Trial of Diffuse Optical Spectroscopic Imaging. *Cancer Res.* **2016**, *76*, 5933–5944. [[CrossRef](#)] [[PubMed](#)]
37. Wang, J.; Pogue, B.W.; Jiang, S.; Paulsen, K.D. Near-infrared tomography of breast cancer hemoglobin, water, lipid, and scattering using combined frequency domain and cw measurement. *Opt. Lett.* **2010**, *35*, 82–84. [[CrossRef](#)]
38. Cerussi, A.E.; Warren, R.; Hill, B.; Roblyer, D.; Leproux, A.; Durkin, A.F.; O’Sullivan, T.; Keene, S.; Haghany, H.; Quang, T.; et al. Tissue phantoms in multicenter clinical trials for diffuse optical technologies. *Biomed. Opt. Express* **2012**, *3*, 966–971. [[CrossRef](#)] [[PubMed](#)]
39. Bosschaart, N.; Leproux, A.; Abdalsalam, O.; Chen, W.-P.; McLaren, C.E.; Tromberg, B.J.; O’Sullivan, T. Diffuse optical spectroscopic imaging for the investigation of human lactation physiology: A case study on mammary involution. *J. Biomed. Opt.* **2019**, *24*, 1–8. [[CrossRef](#)]
40. Biswal, N.C.; Xu, Y.; Zhu, Q. Imaging tumor oxyhemoglobin and deoxyhemoglobin concentrations with ultrasound-guided diffuse optical tomography. *Technol. Cancer Res. Treat.* **2011**, *10*, 417–429. [[CrossRef](#)]
41. Zhu, Q.; Huang, M.; Chen, N.; Zarfos, K.; Jagjivan, B.; Kane, M.; Hedge, P.; Kurtzman, S.H. Ultrasound-Guided Optical Tomographic Imaging of Malignant and Benign Breast Lesions: Initial Clinical Results of 19 Cases. *Neoplasia* **2003**, *5*, 379–388. [[CrossRef](#)]
42. Larusson, F.; Fantini, S.; Miller, E. Hyperspectral image reconstruction for diffuse optical tomography. *Biomed. Opt. Express* **2011**, *2*, 946–965. [[CrossRef](#)]
43. Eames, M.; Wang, J.; Pogue, B.W.; Dehghani, H. Wavelength band optimization in spectral near-infrared optical tomography improves accuracy while reducing data acquisition and computational burden. *J. Biomed. Opt.* **2008**, *13*, 054037. [[CrossRef](#)]
44. Brooksby, B.; Dehghani, H.; Pogue, B.; Paulsen, K. Near-infrared (nir) tomography breast image reconstruction with a priori structural information from mri: Algorithm development for reconstructing heterogeneities. *IEEE J. Sel. Top. Quantum Electron.* **2003**, *9*, 199–209. [[CrossRef](#)]
45. Brooksby, B.; Jiang, S.; Dehghani, H.; Pogue, B.W.; Paulsen, K.D.; Weaver, J.; Kogel, C.; Poplack, S.P. Combining near-infrared tomography and magnetic resonance imaging to study in vivo breast tissue: Implementation of a Laplacian-type regularization to incorporate magnetic resonance structure. *J. Biomed. Opt.* **2005**, *10*, 051504. [[CrossRef](#)] [[PubMed](#)]

